fuels

MDPI

Article

A Multiscale CFD Model of Evaporating Hydrogen Menisci: Incorporating Subgrid Thin-Film Dynamics and In Situ Accommodation Coefficients

Ayaaz Yasin [†], Saaras Pakanati [†] and Kishan Bellur [*]

Department of Mechanical and Materials Engineering, University of Cincinnati, Cincinnati, OH 45220, USA; yasinaz@mail.uc.edu (A.Y.); pakanass@mail.uc.edu (S.P.)

* Correspondence: bellurkn@ucmail.uc.edu

† These authors contributed equally to this work.

Abstract

Due to its high energy density, liquid Hydrogen is an essential fuel for both terrestrial energy systems and space propulsion. However, uncontrolled evaporation poses a challenge for cryogenic storage and transport technologies. Accurate modeling of evaporation remains difficult due to the multiscale menisci formed by the wetting liquid phase. Thin liquid films form near the walls of containers, ranging from millimeters to nanometers in thickness. Heat conduction through the solid walls enables high evaporation rates in this region. Discrepancies in the reported values of the accommodation coefficients (necessary inputs to models) further complicate evaporation calculations. In this study, we present a novel multiscale model for CFD simulations of evaporating Hydrogen menisci. Film profiles below 10 µm are computed by a subgrid model using a lubrication-type thin film equation. The microscale model is combined with a macroscale model above 10 µm. Evaporation rates are computed using a kinetic phase change model combined with in situ calculations of the accommodation coefficient using transition state theory. The submodels are implemented in Ansys Fluent^{TM} using User-Defined Functions (UDFs), and a method to establish two-way coupling is detailed. The modeling results are in good agreement with cryo-neutron experiments and show improvement over prior models. The model, including UDFs, is made available through a public repository.

Keywords: evaporation; thin film; computational fluid dynamics; hydrogen; accommodation coefficient; kinetic theory; multiscale modeling; phase change

Academic Editor: Javier Ereña

Received: 16 October 2025
Revised: 11 November 2025
Accepted: 8 December 2025
Published: 12 January 2026

1. Introduction

Hydrogen is a commonly used rocket propellant [1,2] and is poised to fuel the next generation of green energy systems on Earth [3–7]. Its cryogenic nature poses significant challenges for storage technologies [8–12]. During extended space missions, such as interplanetary flights, heat leakage to storage tanks can cause substantial fuel loss due to evaporation [13]. The development of technologies to reduce evaporative loss necessitates an ability to model evaporation mass and heat transfer in such fuel systems [14].

Fuel systems consist of single-species liquid and vapor phases, where molecular interactions at the liquid-vapor interface describe phase change processes [15–17]. In contrast, phase change in systems with multi-species vapor phases is dominated by diffusive resistance [18–20]. The kinetic theory of gases has long been used to study liquid-vapor phase change in single-species systems [21]. The classical Hertz-Knudsen-Schrage

equation [22–24] predicts interphase mass transfer for planar interfaces. Modifications to the equation were provided by Wayner et al. [25] and most recently by Bellur et al. [26] to incorporate the effects of curved interfaces,

$$\dot{m}'' = \frac{2\alpha_c}{2-\alpha_c}\sqrt{\frac{M}{2\pi\overline{R}T_v}}p_v\left[\beta W\sqrt{\frac{T_v}{T_i}}-1\right] \tag{1}$$

$$\text{where, } W = \frac{p_v^{\text{sat}}}{p_v} + \left(1-\frac{T_v}{T_i}\right)\left(\frac{p_v^{\text{sat}}h_{\text{fg}}}{p_v}\right) + \left(\frac{T_v}{T_i}\right)\left(\frac{\rho_v^{\text{sat}}}{\rho_l}\right)\left(\frac{\Pi+\sigma\kappa}{p_v}\right)$$

where, M is the molar mass, $\overline{R}$ is the universal gas constant, h_{fg} is the latent heat of vaporization, T_v and T_i are the vapor and interface temperatures, respectively, p_v is the vapor pressure, ρ_v and ρ_l are the densities of the vapor and liquid phases, respectively, σ is the surface tension, and κ is the mean curvature of the interface. The superscript *sat* denotes saturation properties at T_v. Disjoining pressure, an intermolecular attractive force between the solid wall and the vapor phase, is denoted by Π and further discussed in Section 2. α_e and α_c are the evaporation and condensation accommodation coefficients, respectively, and their ratio $\beta = \alpha_e/\alpha_c$ may be assumed to be close to unity [27]. Values of the accommodation coefficient, hereafter denoted by α, are necessary inputs to kinetic phase change models. However, close to a century of experimental studies show orders of magnitude of variation for common fluids [28,29]. Although the accommodation coefficient is often assumed to be constant [30,31], molecular dynamics studies have shown variation in its values due to temperature [32–34]. Experimental data for cryogenic fluids remains limited [26].

1.1. Cryo-Neutron Experiments

To help understand phase change in cryogenic fluids and provide data for accommodation coefficients, Bellur et al. [35,36] conducted a series of experiments where phase change in cryogenic Hydrogen and Methane was measured using neutron imaging. Cylindrical test cells made of Al 6061 and SS 316 were placed inside a cryostat. Hydrogen vapor was introduced, and the heater temperature was controlled to induce condensation, followed by evaporation. The liquid volume was imaged using a neutron beamline every 10 s. Neutron images were analyzed to calculate the total phase change rate as a function of time [37]. Figure 1 shows the changing liquid volume inside the test cell and the ability to measure evaporation and condensation rates. The data was then published in a publicly available data repository [36]. This data serves as an ideal testbed for the evaporation model developed herein.

Analysis of the experimental image data of the Hydrogen meniscus shows high interface curvature and a low contact angle [37,38]. Due to the low evaporation rates in the Hydrogen experiments (16 to 885 µg/s) [36], the meniscus shape was found to match solutions to the Young-Laplace equation for static menisci in right circular cylinders derived by Concus [39],

$$\left.\begin{aligned}\frac{d\tilde{f}}{d\psi} &= \frac{\sin\psi}{\text{Bo}\,\tilde{f}-(\sin\psi)/\tilde{r}+\lambda}\\ \frac{d\tilde{r}}{d\psi} &= \frac{\cos\psi}{\text{Bo}\,\tilde{f}-(\sin\psi)/\tilde{r}+\lambda}\end{aligned}\right\}\quad \psi\in\left[0,\frac{\pi}{2}-\theta\right] \tag{2}$$

where, $\tilde{r} = r/R$ is the non-dimensional radial position for a cylindrical container of radius R, $\tilde{f}$ is the non-dimensional height of the meniscus in the axial direction above the apex, $\text{Bo} = \rho_l g R^2/\sigma$ is the Bond number for gravitational acceleration g, $\psi = \tan^{-1} d\tilde{f}/d\tilde{r}$ is the

slope angle, and λ is twice the curvature at the apex of the meniscus determined through a numerical procedure described by Concus [39]. θ is the contact angle of the meniscus. Experimentally measured value of $\theta = 0$ is used for Hydrogen [38].

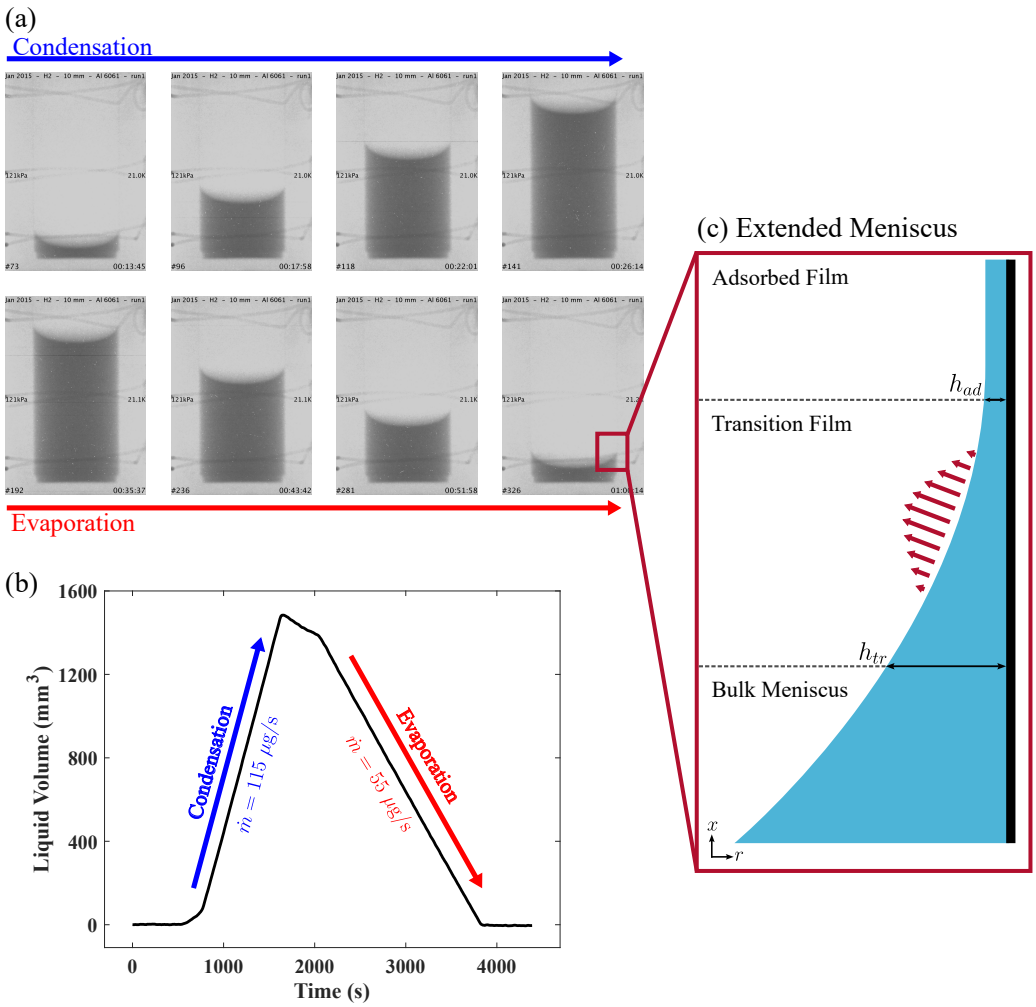

Figure 1. (**a**) Selected neutron images from the Hydrogen 10 mm Al test cell [36]. (**b**) The change in liquid volume as a function of time was used to calculate the total evaporation rate [36]. (**c**) Three regions of the liquid-vapor are delineated as a function of film thickness, h. The transition thin film region near the solid wall experiences high evaporation fluxes.

Evaporation along the menisci of cryogenic fuels is anticipated to be non-uniform due to the high surface curvature of the interface and increased heat transfer near the container walls [40]. The low contact angles formed by liquid Hydrogen [38] result in an *extended meniscus* region, where the liquid film height ranges from millimeters to nanometers. The liquid-vapor meniscus can be delineated into three distinct regions (Figure 1c) [41]. Far from the solid wall, the bulk meniscus region experiences curvature due to capillary forces. In this region, the meniscus shape is described by Equation (2). However, within a few micrometers of the solid wall, the increasing interaction between solid and vapor molecules, due to disjoining pressure, results in a transition thin film region. Here, the diminishing capillary pressure and increased heat conduction from the wall result in high evaporation fluxes [16,26,41–43]. Within nanometers from the wall, disjoining pressure dominates, and a non-evaporating film of constant thickness forms, also known as the adsorbed film. With varying length-scales and dominant physical phenomena, modeling approaches differ across these regions. While the *extended meniscus* region is a small fraction of the total surface area, its contribution to the overall phase change rate is significant [16]. However,

the multiscale nature of this problem poses a limitation for traditional CFD models, which exacerbate the preexisting challenges that arise from the use of tuning parameters in kinetic phase change models [28,44,45].

1.2. Bulk Meniscus Models

Attempts to include a phase change model into a computational fluid dynamics framework date back to Lee [46]. Lee's model is widely used in commercial software packages [47,48]. It calculates the local interphase mass transfer based on the deviation of the interface temperature from the saturation temperature. This approach neglects pressure contributions to the phase change mass transfer and relies heavily on tuning coefficients [44]. Due to its dependence on computational and physical parameters, the values of the Lee coefficients are difficult to predict and vary significantly for similar physical regimes and applications [49]. In recent review articles, Kharangate and Mudawar [50] and Kim et al. [51] reported values of the Lee coefficients ranging from eight to nine orders of magnitude, respectively. More recent work has extended this discrepancy to ten orders of magnitude [52]. This shows that despite its widespread use, the Lee model is inherently flawed due to its reliance on seemingly arbitrary tuning parameters.

To eliminate the reliance on tuning parameters, in a prior study [49], the authors built a CFD routine to compute the evaporation mass flux along the bulk meniscus using Equations (1) and (5). It was found that the vapor temperature obtained from the CFD calculations needs to be reduced to match the vapor temperature in the Knudsen layer, which is required as input to the kinetic equations. While CFD methods are unable to resolve the sub-continuum temperature gradients, molecular dynamics studies have corroborated temperature deviations in the Knudsen layer due to the non-equilibrium effects of phase change [34,53–55]. Gatapova [56] measured Knudsen layer temperatures experimentally during the evaporation process and found similar temperature gradients. The *macroscale bulk model* developed by the authors [49] introduced the reduction factor $\gamma \in [0, 1)$ such that,

$$T_v^* = T_v(1 - \gamma) \tag{3}$$

where T_v is the vapor temperature obtained from the CFD solution, and T_v^* is the reduced vapor temperature used as an input to Equation (1). The overall evaporation rate was found to be a strong function of γ. The authors [49] used data from the cryo-neutron experiments [35] (Section 1.1) to determine values of γ, reporting a predictable, species-independent relation between the evaporating molar flux and γ,

$$\gamma = c_1(\exp(c_2 J_M) - 1), \qquad \text{where, } J_M = \frac{\dot{m}}{M \times A_{\text{surf}}} \tag{4}$$

where J_M is the area-averaged molar flux, A_{surf} is the surface area of the liquid-vapor interface, and c_1 and c_2 are obtained through a methodology described in Ref. [49]. The meniscus in the CFD domain was constructed using Equation (2); however, the meniscus was terminated at a distance of 10 µm from the wall, introducing a *cutoff* as detailed in Section 3. Below this length scale, the evaporation was not modeled, i.e., the transition thin film was not modeled. The micrometer length scales cannot be resolved by the computational meshes used in CFD simulations. To avoid this, simplified lubrication-type models are used to compute the interface shape and evaporation rates in the thin film [57].

1.3. Transition Thin Film Models

To model the microscale thin film region, a common approach is to take derivatives of the Young-Laplace equation (Equation (6)) to derive a differential equation describing the height profile of the liquid-vapor interface (h in Figure 1c). This nonlinear differential equa-

tion is commonly referred to as an *evolution equation* (Equation (8)) [58]. The low Reynolds and capillary numbers in thin film flows enable the inertial terms to be neglected [59]. The sufficiently low aspect ratio (characteristic height to characteristic length, $\varepsilon = H/L$) of the transition thin film region allows the Navier-Stokes equations to be reduced by using the lubrication approximation [60].

This approach has been extended to evaporating films with heat transfer effects [61–63]. Similar to the hydrodynamic effects, the heat transfer is also reduced to a one-dimensional approximation and coupled with a kinetic phase change model, which supplies the thermal boundary condition at the liquid-vapor interface, accounting for the latent heat loss [42,57,64–66]. The evolution equation and the thermal-evaporation equations are solved in tandem [16,67]. The mathematical derivation of the model used in the present study is described in Section 2.

Transition thin film models commonly suffer from non-physical assumptions and guessed boundary conditions [42,65,68–77]. These are generally not known *a-priori* leading to a wide array of simplifications, guesses, and tuning to attain numerical stability as described below.

- Adsorbed film boundary conditions such as h_{ad}, h_x and h_{xx} are not known *a-priori*. Most prior studies commonly guess or tune these boundary conditions to attain a numerically stable solution.
- Bulk curvature boundary conditions are generally not readily available. A common approach is to tune adsorbed film boundary conditions to match an arbitrary bulk curvature.
- Thermal boundary conditions are generally set as a constant superheat, which forces a uniform isothermal wall temperature condition.
- Mass flux boundary conditions are needed at either h_{ad} and h_{tr} (Figure 1c), but these are also unknown, leading to more tuning parameters.

There have been attempts to develop new approaches to thin film modeling that avoid the assumptions listed above [16,76]. However, their applicability is limited to the thin film region. Coupling to the bulk region, such as a CFD solution, remains a challenge. This is particularly difficult since the model must satisfy continuity in the interface shape and mass flux between the bulk meniscus and transition thin film regions.

1.4. Issues with Multiscale Models

Coupling the bulk meniscus solution to the transition thin film has proved challenging. Boundary conditions at the adsorbed film are difficult to determine experimentally, and a common approach for numerical models has been to guess the adsorbed film boundary conditions using a shooting method until a match with the bulk meniscus can be established [68,78,79]. To avoid guessed boundary conditions, some researchers have started their solution from the intersection of the bulk meniscus and the transition thin film region [76,78,80–82] (Figure 1c).

Bellur et al. [16] developed a multiscale model in which the bulk meniscus shape was computed using Equation (2), but the solution was truncated at a distance of 10 µm from the solid wall. A separate transition thin film model was solved starting at 10 µm using the derivatives (h_x, h_{xx}) from the bulk interface shape. Abolmaali et al. [73] recently developed a method where the transition thin film is solved using a lubrication-type model and meshed along with the bulk meniscus for a liquid-only CFD simulation. While this approach allows the regions to be coupled, the mesh limitations prohibit its application to systems larger than 100 µm. Furthermore, these studies do not establish a two-way coupling between the microscale and macroscale models.

This mismatch in the modeling approach between the bulk meniscus and transition thin film regions presents a key hurdle for cryogenic fuels, where evaporation in the transition thin film is known to be significant [16,21]. A method to solve the transition thin film region and its evaporation contribution with two-way coupling in a CFD simulation remains lacking.

1.5. Present Study

In the present study, we develop a method to model a multiscale evaporating liquid-vapor interface in a two-phase CFD simulation without the arbitrary tuning of parameters. Evaporation is modeled using Equation (1). The value of the accommodation coefficient, α, is evaluated based on transition state theory [83],

$$\alpha = (1-\ell)\exp\left(\frac{-\ell}{2(1-\ell)}\right), \qquad \ell = \sqrt[3]{\frac{\rho_v}{\rho_l}} \tag{5}$$

Equation (5) has been validated by molecular dynamics simulations and by experimental data for cryogenic fluids [26,55,84,85] (Figure 2). This makes α a density-dependent fluid property. Using densities from the CFD simulation allows α to be calculated in situ, removing its use as a tuning parameter.

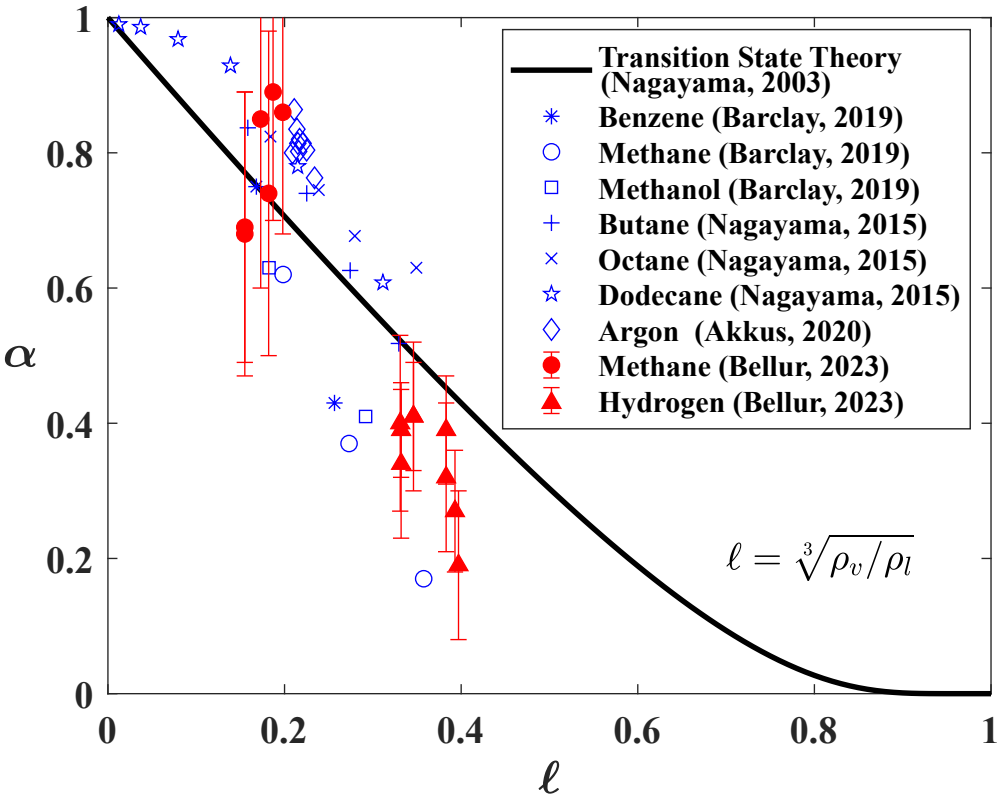

Figure 2. Accommodation coefficient data from molecular dynamics [55,84,85] and experimental studies [26] with various hydrocarbons showing a comparison with values predicted by Equation (5) [83].

The simulation is set up in Ansys Fluent™ 2023 R2, and User-Defined Functions (UDFs) are used to implement a subgrid microscale thin film model. Solid wall temperatures are extracted from the macroscale CFD calculations and used as inputs to the microscale model, which includes the transition thin film region. Enhanced evaporation from the microscale model is returned to the macroscale CFD model through heat and mass source terms. Thus, a two-way coupling is enforced between the microscale and macroscale models. The microscale model consists of a numerical ODE solution evaluated at each CFD

iteration. A numerical treatment is provided in Section 3 to ensure convergence of both the macroscale CFD simulation and the subgrid microscale model. The macroscale model developed by Yasin and Bellur [49] is used to capture evaporation at length scales above 10 µm. The combined multiscale approach is used to simulate the cryo-neutron experiments. Due to the low evaporation rates observed by the experiments [21,36,49], a quasi-steady state approximation is made to reduce the computational complexity. Evaporation rates from the computational model are compared with experimental measurements in Section 4, and the distribution of mass transfer rates between the bulk meniscus and the transition thin film is discussed. The implementation of the subgrid microscale model in Ansys Fluent™ is discussed in Section 3, and the mathematical derivation is provided in Section 2.

2. Microscale Thin Film Model

In the transition thin film region, the augmented Young-Laplace equation [25] describes the pressure balance along the liquid-vapor interface,

$$p_v - p_l = \sigma\kappa + \Pi \tag{6}$$

where p_v and p_l are the vapor and liquid pressures, respectively. The curvature of the interface in cylindrical coordinates is,

$$\kappa = h_{xx}(1+h_x^2)^{-3/2} + (R-h)^{-1}(1+h_x^2)^{-1/2} \tag{7}$$

where R is the radius of the cylindrical container and h is the thickness of the liquid film, i.e., the distance between the liquid-vapor interface and the solid wall in the r-direction (Figure 3). Substituting Equation (7) into Equation (6) and differentiating along the axial length of the cylindrical container provides a nonlinear evolution equation for the thin film,

$$h_{xxx} - \frac{3h_x h_{xx}^2}{1+h_x^2} - \frac{h_x h_{xx}}{R-h} + \frac{h_x(1+h_x^2)}{(R-h)^2} + \left(\frac{1+h_x^2}{R-h} + h_{xx}\right)\frac{1}{\sigma}\frac{d\sigma}{dx} + \frac{(1+h_x^2)^{3/2}}{\sigma}\left(\frac{dp_l}{dx} + \frac{d\Pi}{dx}\right) = 0 \tag{8}$$

Here, surface tension is a function of the interface temperature, T_i,

$$\frac{d\sigma}{dx} = \sigma_T \frac{dT_i}{dx} \tag{9}$$

where $\sigma_T = \dfrac{d\sigma}{dT}$ is a property of the liquid phase. The relationship between disjoining pressure and h is indicated by experiments [86] as,

$$\Pi = \frac{\mathcal{A}}{h^3} \tag{10}$$

where $\mathcal{A}$ is the Hamaker constant. A value of 5.11×10^{-21} J is used for Hydrogen [87]. Equation (10) is found to be appropriate for the current case [16]; however, alternate disjoining pressure models [88] may be used in this framework.

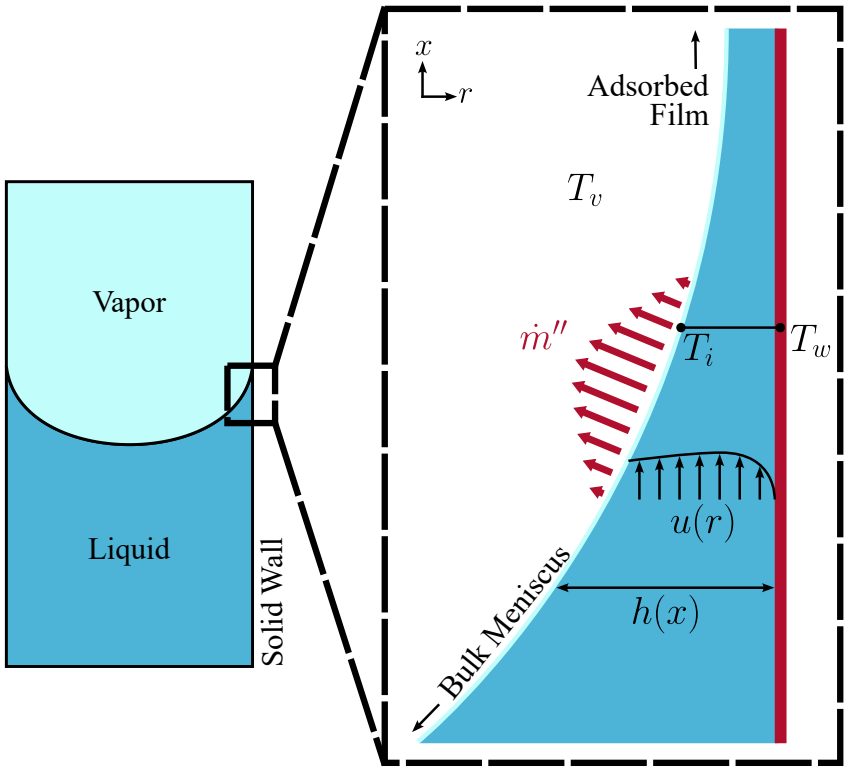

Figure 3. A geometrical representation of the transition thin film with important parameters of the microscale model.

2.1. Interface Temperature and Mass Flux

To calculate the interfacial temperature, the steady-state heat equation is used,

$$k_l \frac{\partial}{\partial r}\left(r \frac{\partial T}{\partial r}\right) = 0 \tag{11}$$

A Dirichlet boundary condition is used at the wall, describing the wall temperature provided by the CFD simulation, which is supplied to the UDF as a continuous first-order function, $T_w(x)$ (Section 3). A Neumann boundary condition is used at the interface to account for heat conduction losses due to latent heat. The boundary conditions can be represented as,

$$\text{at } r = R, \qquad T = T_w$$

$$\text{at } r = R - h, \quad k_l \frac{\partial T}{\partial r} = \dot{m}'' h_{\text{fg}}$$

where k_l is the thermal conductivity of the liquid phase. The interfacial temperature distribution is then obtained,

$$T_i(x) = T_w(x) - \dot{m}''(x) \frac{h_{\text{fg}}}{k} (R - h(x)) \ln\left(\frac{R}{R - h(x)}\right) \tag{12}$$

Equation (1) is used to calculate the evaporation mass flux. T_v is reduced using γ (Equation (3)). A universal value of γ is used between the microscale and macroscale models. Equation (12) is solved iteratively along with Equation (1) to obtain a converged interface temperature, T_i, and evaporation mass flux, $\dot{m}''$. Due to the nonlinear relationship between T_i and $\dot{m}''$, an under-relaxation factor of 0.1 is used for T_i to ensure convergence.

2.2. Lubrication Approximation

The Navier-Stokes equations are reduced under the lubrication approximation,

$$\frac{1}{r}\frac{\partial}{\partial r}\left(r\frac{\partial u}{\partial r}\right) = \frac{1}{\mu}\frac{dp_l}{dx} \tag{13}$$

where u is the liquid velocity in the x-direction (Figure 3). Equation (13) is integrated analytically, using a no-slip boundary condition at the solid wall and surface tension-driven Marangoni stress at the interface,

$$\text{at } r = R, \qquad u = 0$$

$$\text{at } r = R - h, \quad -\mu\frac{\partial u}{\partial r} = \sigma_T\frac{dT_i}{dx}$$

resulting in the velocity profile through the thin film, $u(r)$,

$$u(r) = \frac{R-h}{2\mu}\left(\frac{R+h}{2} + (R-h)\ln\frac{R}{r}\right)\frac{\partial p_l}{\partial x}(x) + \left(\frac{R-h}{\mu}\ln\frac{R}{r}\right)\sigma_T\frac{\partial T_i}{\partial x}(x) \tag{14}$$

To reduce the computational load in the microscale model, the mass flow Γ through the thin film is analytically integrated using Equation (14), to obtain its relationship with the liquid pressure gradient $\frac{dp_l}{dx}$,

$$\Gamma(x) = 2\pi\rho_l\int_{R-h}^{R} u(r)\, r\, dr \tag{15}$$

$$\frac{\partial p_l}{\partial x}(x) = \frac{\frac{4\sigma_T}{R-h}\frac{\partial T_i}{\partial x}\left(1 - 2\ln\frac{R}{R-h}\right) - \frac{8\mu\Gamma}{\pi\rho_l}\frac{1}{h(2R-h)(R-h)^2}}{1 + 2\left(1 - 2\ln\frac{R}{R-h}\right) + \frac{R^2}{(R-h)^2}} \tag{16}$$

2.3. Numerical Solution

Equations (9), (10), (12) and (16) are solved simultaneously with Equation (8) using a fourth-order Runge–Kutta method, similar to previous studies [16,67]. The solution starts at $h = 10$ µm, with initial values of h_x and h_{xx} obtained from the bulk meniscus shape (Equation (2)) to ensure C^2 continuity in the interface shape. The values of h_{fg}, k_l, ρ_l, μ_l, and σ are calculated as functions of T_i, and ρ_v is calculated as the saturation density at T_v using curve fits of data obtained from the NIST Standard Reference Database [89]. Wall temperature data from the previous CFD iteration are fitted to obtain a continuous function $T_w(x)$, which is used as the thermal boundary condition in the current iteration. A fixed step-size of $\Delta x = 10^{-8}$ m was used due to the high stiffness of the thin film evolution equation and to provide adequate resolution near the adsorbed region, where film height is anticipated to be $\sim 10^{-7}$ m and $\dot{m}''$ undergoes large gradients. The solution is terminated when $\dot{m}'' = 0$ within a tolerance of 10^{-5} kg/m^{2}s. Algorithm 1 describes the logical flow of the microscale model. Algorithm 2 describes the computation of the derivative function required for the numerical integration in step 5 of Algorithm 1.

Algorithm 1 Logical flow of the microscale model

1: **Input:** Initial h, h_x, h_{xx} at $x_o = 0$ from the bulk meniscus, wall temperature data from CFD, p_v, A, M, material properties (h_{fg}, k_l, ρ_l, ρ_v, μ_l, σ) as functions of temperature and, reduction factor γ.
2: **Set:** Step-size $\Delta x = 10^{-8}$ m.
3: **Define:** $T_w(x)$ as a curve-fit of the CFD wall temperature data.
4: **Define:** $H_o = \{h, h_x, h_{xx}\}$ at $x_o = 0$.
5: **Solve:** The initial value problem using fourth-order Runge–Kutta, with initial conditions (x_o, H_o), and derivative function `evolution` (Algorithm 2).
6: **Terminate:** The Runge–Kutta loop, when $\dot{m}'' = 0$.
7: **Calculate**: S_m and S_{HB} using Equations (21) and (23), respectively.
8: **Return:** S_m and S_{HB} to CFD simulation.

Algorithm 2 `evolution` function used in step 5 of Algorithm 1. The `evolution` function inputs x and $H = \{h, h_x, h_{xx}\}$ for the current Runge–Kutta step and returns the derivative $H_x = \{h_x, h_{xx}, h_{xxx}\}$

1: **Input:** (x, H), $T_w(x)$, p_v, A, M, material properties (h_{fg}, k_l, ρ_l, ρ_v, μ_l, σ) as functions of T and, reduction factor γ.
2: **Calculate:** T_v^* using T_v and γ as inputs to Equation (3).
3: **Solve:** Iterate Equations (1) and (12) using T_v^* until T_i converges to a tolerance of 10^{-4}.
4: **Calculate:** α using ρ_v and ρ_l as inputs to Equation (5).
5: **Calculate:** The interfacial temperature gradient using a finite-difference between the current and previous Runge–Kutta steps, $\dfrac{dT_i}{dx} = \dfrac{T_i^x - T_i^{x-\Delta x}}{\Delta x}$.
6: **Calculate:** The disjoining pressure gradient using h and h_x, $\dfrac{d\Pi}{dx} = -\dfrac{3Ah_x}{h^4}$.
7: **Calculate:** The surface tension gradient, $\dfrac{d\sigma}{dx} = \sigma_T \dfrac{dT_i}{dx}$
8: **Calculate:** Liquid pressure gradient using σ_T, T_i, Γ, and ρ_l as inputs to Equation (16).
9: **Calculate:** h_{xxx} using h, h_x, h_{xx}, R, σ, $\dfrac{d\sigma}{dx}$, $\dfrac{dp_l}{dx}$ and, $\dfrac{d\Pi}{dx}$ as inputs to Equation (8).
10: **Return:** $H_x = \{h_x, h_{xx}, h_{xxx}\}$.

3. Multiscale Coupling

The microscale evaporation model is implemented within an Ansys Fluent™ 2023 R2 CFD simulation using User-Defined Functions (UDFs). All simulations are run using a steady-state SIMPLEC solver with a laminar viscous model due to the low evaporation rates, which result in low velocity gradients. This section details the two-way coupling established between the CFD simulation and the microscale evaporation model. At each iteration of the CFD simulation, temperatures from the solid wall adjacent to the *cutoff* (Figure 4d) are extracted, tagged with their respective x-locations, and sent to the microscale evaporation model (Algorithm 1). When the microscale model is evaluated, the evaporating mass and the associated latent heat loss are returned to the CFD simulation as source terms to be implemented at the current iteration. Ansys Fluent™ solves the governing equations in volumetric form [47],

$$\nabla \cdot \vec{u} = S_m \tag{17}$$

$$\rho(\vec{u} \cdot \nabla)\vec{u} = -\nabla p + \mu \nabla^2 \vec{u} + \rho \vec{g} \tag{18}$$

$$\rho \nabla \cdot (\vec{u} H_s) = k \nabla^2 T + S_{HB} \qquad \text{where} \quad H_s = \int_{T_{ref}}^{T} c_p \, dT \tag{19}$$

where $\vec{u}$ is the velocity, $\vec{g}$ is the gravitational acceleration, c_p is the specific heat, and H_s is the sensible enthalpy of the respective phase. S_m is a mass source term used to add the

evaporating mass to the vapor phase. The mass flux distribution along the transition thin film solution is integrated to calculate the source terms.

$$S_m = \frac{1}{V_{\text{cell}}} \iint_S \dot{m}'' dA \tag{20}$$

$$\approx \frac{\pi}{V_{\text{cell}}} \sum_{j=1}^{N} \dot{m}_j'' \left[(R - h_{j+1}) - (R - h_j) \right] \left[(h_{j+1} - h_j)^2 + (x_{j+1} - x_j)^2 \right]^{1/2} \tag{21}$$

where N is the number of Runge–Kutta steps in the microscale solution and V_{cell} is the cell volume of the vapor mesh cell adjacent to the *cutoff* where the evaporating mass is added (Figure 4d). For the integral in Equation (19), Ansys Fluent™ uses a reference temperature, $T_{\text{ref}} = 298.15$ K. Therefore, to set the temperature of the evaporating mass, a heat balance source term, S_{HB}, is used in Equation (19), which accounts for both the reference temperature correction and the latent heat. The evaporating mass is added at the mass flux–averaged interface temperature, $\overline{T_i}$, of the transition thin film to account for latent heat.

$$\overline{T_i} = \frac{\int_0^L \dot{m}''(x)\, T_i(x)\, dx}{\int_0^L \dot{m}''(x)\, dx} \approx \frac{\sum_{j=1}^{N} \dot{m}_j''\, T_i(x_j)}{\sum_{j=1}^{N} \dot{m}_j''} \tag{22}$$

$$S_{\text{HB}} = -S_m c_p (T_{\text{ref}} - \overline{T_i}) \tag{23}$$

To promote convergence between the CFD simulation and the microscale model, an iterative routine is established (Figure 5). The CFD simulation with the macroscale meniscus model is run for the first 100 iterations with no source terms from the microscale model. This allows temperatures near the cutoff to approach physical and stable values. The microscale model is then executed at every fifth iteration of the CFD simulation to calculate and update the source terms, S_m and S_{HB}. The source terms are held fixed for the next four iterations, and the CFD simulation is allowed to partially converge. After five iterations, the microscale model is executed again, and the process is repeated. Executing the microscale model every fifth iteration allows for the CFD simulation to attain a pseudo-converged state at the previous value of the source terms before they are updated again. This feature is vital to overall stability as the CFD simulation requires more iterations than the microscale model to converge. If the source terms were updated in every iteration, the CFD solution lags behind and is always trying to catch up with the rapidly changing microscale model, posing a threat to numerical stability. The convergence of the overall solution is monitored by the residuals of the CFD simulation, which are allowed to reach 10^{-3} before the solution data is extracted. On average, it took 1000 iterations to achieve this residual limit across all simulations. However, it is vital to note that Fluent residuals are normalized. Results from simulations of the cryo-neutron experiments and comparison with prior studies are discussed in the following section.

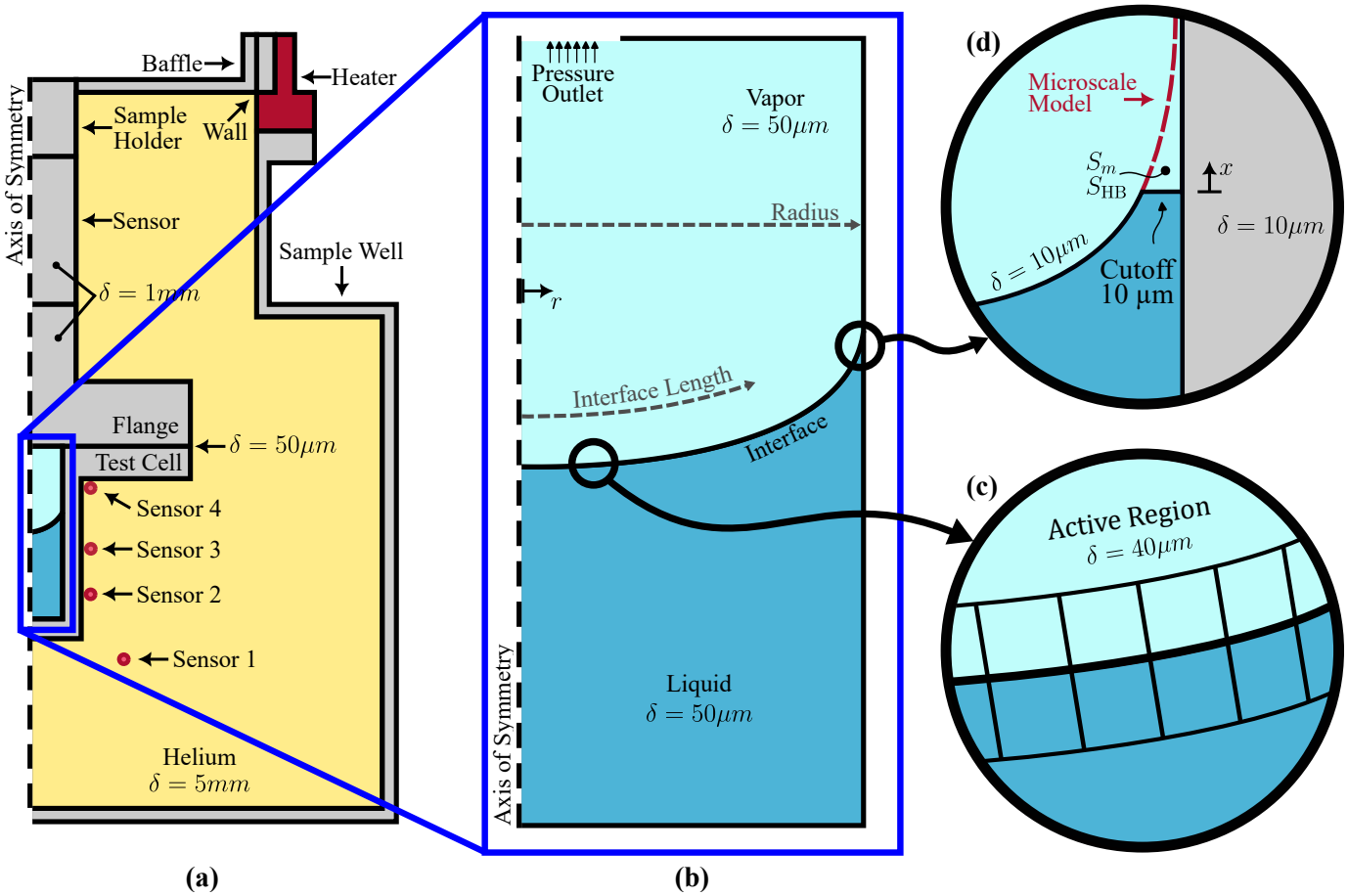

Figure 4. The CFD domain of the cryo-neutron experimental setup is visualized. The approximate mesh cell sizes in a region are shown as values of δ. (**a**) The relative position of the elements within the cryostat is shown. The approximate locations of the thermocouples (Sensors 1–4) used to characterize the heat transfer through the domain (Section 4.1) are shown. To scale drawings of the CFD domain are available in the supplementary material of Ref. [49], and precise locations of the thermocouples are available in Ref. [35]. (**b**) The bulk meniscus shape is obtained from solutions to Equation (2). (**c**) The computational mesh is structured along the meniscus to implement the macroscale evaporation model. (**d**) The meniscus is terminated at a distance of 10 μm from the wall and a *cutoff* is introduced. The transition thin film region below 10 μm is shown with a dashed line. Source terms from the microscale model are implemented in the vapor phase adjacent to the *cutoff* to simulate the transition thin film.

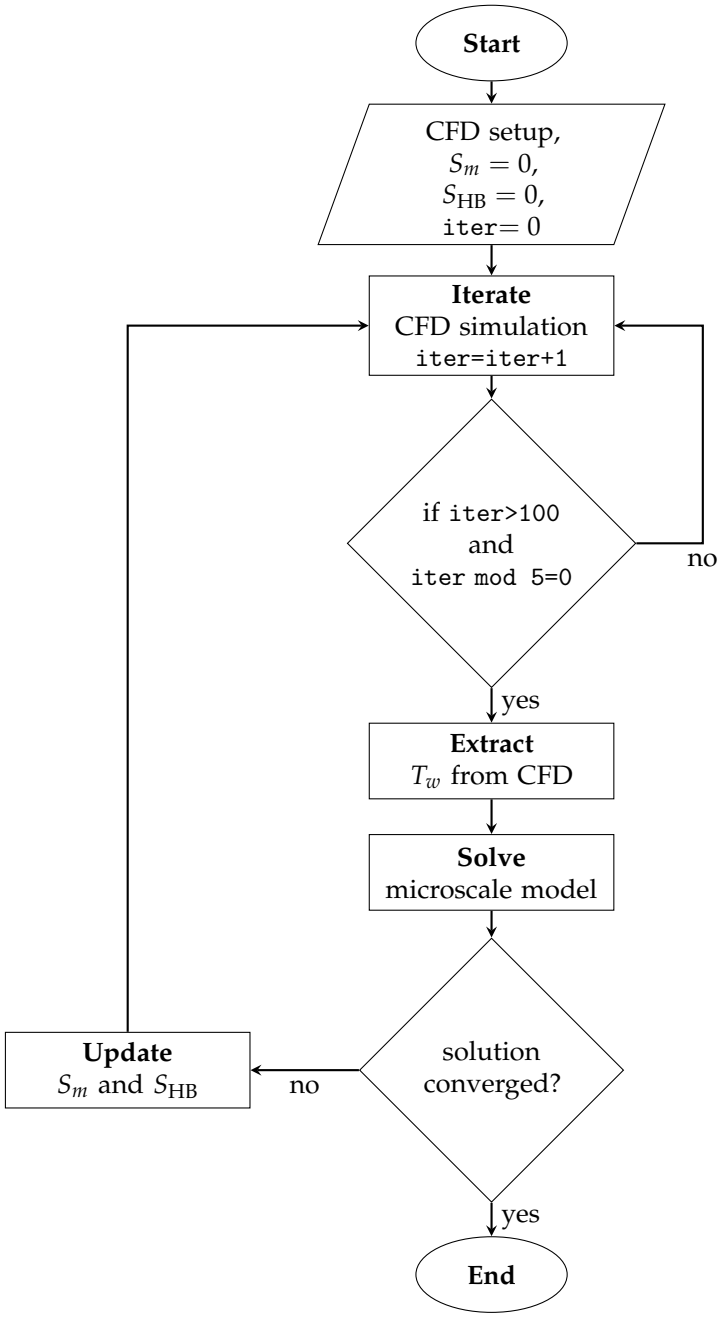

Figure 5. Flowchart describing the two-way coupling between the CFD simulation and the microscale model. The microscale model is implemented within the CFD simulation framework and is updated every 5th iteration. Convergence is said to be achieved when all CFD residuals are below 10^{-3}.

4. Results and Discussion

CFD simulations of the cryo-neutron experiments (Section 1.1) are performed in Ansys Fluent^{TM}. Contact resistances were applied at all solid-solid interfaces inside the cryostat environment [90]. The current work uses data from the 10 mm diameter cylindrical test cells made of SS 316 (tc2) and Al 6061 (tc4) obtained from the experimental dataset [36]. The heat transfer from the heater to the test cell is first validated with "dry" tests conducted with an evacuated cell, and the multiscale model is then applied for the "wet" tests, which involved liquid-vapor phase change.

4.1. Validation with "Dry" Cell Tests

To validate the mesh and ensure that heat transfer is accurately captured, "dry" test data from the experimental dataset [36] is used. In a "dry" test, the test cell was completely evacuated, and the cryostat was subjected to heating and cooling cycles while the test cell temperatures were measured. Four sensors, located at various points on the test cell (Figure 4a), recorded the temperatures with an accuracy of ±0.25 K. Thermal cycling tests were performed to characterize the heat transfer characteristics in the absence of Hydrogen, i.e., no phase change. We have reconstructed the cryostat domain based on the data provided by the experimental team [35,36] using an axisymmetric approach as shown in Figure 4a. Using the experimentally set heater temperature as input, the CFD model is run with a 1-second timestep. The mesh refinement was progressively increased till the modeling results matched the experimental results. Figure 6 shows a comparison of the transient time trace of the final mesh as the domain was thermally cycled. Experimental data from the middle sensor (sensor 2) is compared with the corresponding simulation value to show excellent agreement. The simulated sensor temperatures are within the experimental uncertainty. The "dry" test simulations show that the CFD model accurately predicts the thermal-fluid dynamics in the domain.

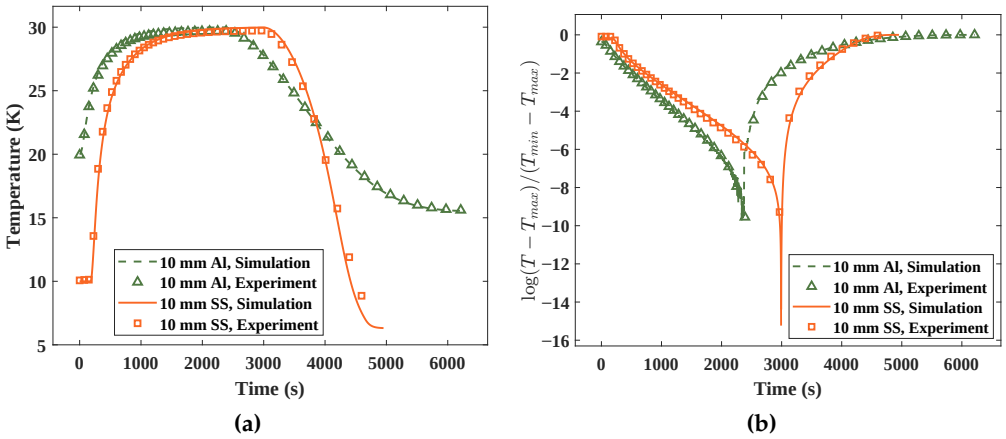

Figure 6. Validation of the thermal response through the CFD domain is performed by comparison with experimental "dry" test data. Data for sensor 2 is shown for the SS 316 (tc2) and Al 6061 (tc4) cells. (**a**) Shows time variation in the sensor temperature. (**b**) Sensor 2 data shown as log-difference.

4.2. Results from "Wet" Cell Tests

Following the "dry" test simulations, the microscale model is implemented in the CFD simulation and coupled as discussed in Section 3. Table 1 details the different cases that were simulated for the 10 mm SS 316 (tc2) and 10 mm Al 6061 (tc4) test cells. In each case, the pressure, heater temperature, and total evaporation rate are available from the experimental dataset [36]. The ultra-low evaporation rates allow for the use of a quasi-steady approximation to simulate an instantaneous moment during the evaporation process (Figure 1). The sensor temperatures, wall temperature in the vicinity of the cutoff, thin film evaporation rate, and vapor mass flow leaving the outlet were used as convergence monitors. Simulation was deemed converged when variations in the temperatures were ±0.005 K and all other quantities were within 0.5% for 100 iterations. This coincided with a continuity residual of 10^{-3} in the Fluent model with Energy residuals below 10^{-6}.

The evaporating mass added to the vapor phase is allowed to leave the domain through the pressure outlet at the top of the test cell. Figure 7 shows the temperature gradient from the heater to the test cell and the evaporation-driven flow patterns in the vapor phase. The non-uniform evaporation flux along the liquid-vapor interface induces recirculation near the heated wall (see Figure 7c). High evaporation rates near the three-phase contact line are

captured by the microscale model, resulting in higher vapor velocities in this region. The overall effect is a jet-like flow of vapor from the vicinity of the contact line to the central outlet, resulting in recirculation near the wall and top corner. Similar flow patterns were observed in the work of Khrustalev and Faghri [91].

Table 1. Results and comparison with experiments and prior computational studies. The experimental results have a 5% error. Evaporation rates, $\dot{m}$, are reported in µg/s. All studies used a *cutoff* length of 10 µm. Bulk and thin film (tf) values refer to contributions from above and below the *cutoff*, respectively.

Cryo-Neutron Experiments [35]				Present Study			Bellur et al. [16]		Yasin and Bellur [49]
Test Cell	**Run**	**Pressure (kPa)**	$\dot{m}_{exp}$	$\dot{m}_{total}$	$\dot{m}_{bulk}$	$\dot{m}_{tf}$	$\dot{m}_{bulk}$	$\dot{m}_{tf}$	$\dot{m}_{bulk}$
tc2 (10 mm SS 316)	1	120.9	16.43	16.40	11.94	4.46	14.17	2.25	16.93
	2	88.32	17.27	17.20	12.83	4.37	14.72	2.49	17.27
	3	201.96	21.39	21.56	16.19	5.36	18.54	2.84	21.40
tc4 (10 mm Al 6061)	1	121.3	55.50	55.26	46.09	9.17	43.74	11.18	54.67
	2	87.9	55.20	55.25	46.14	9.11	43.44	11.75	54.95
	3	200.05	93.12	92.80	79.02	13.78	73.89	19.22	91.71
	4	226.84	77.31	77.84	63.63	14.21	62.85	14.47	—

Figure 8a shows the evaporation mass flux along the entire liquid-vapor interface. This is represented as a function of the normalized interface length (distance from the apex normalized by radius). There is a general increase in the mass flux from the apex of the meniscus towards the contact line, which the model captures. The increase is gradual in the macroscale region, but rapid in the microscale thin film region. The blue dots represent the fluxes extracted from the cell centroids of the macroscale domain. As the film approaches the wall, the CFD mesh begins to experience enhanced skewing, leading to unreliable noise in its values. However, mass flux values from the macroscale and microscale models are in good agreement and exhibit C^0 continuity at the *cutoff* (see Figure 8a inset). The peak mass flux in the thin film region is found to be nearly an order of magnitude greater than the apex of the meniscus, highlighting the importance of the microscale model. The flux quickly reduces to zero as the film thickness approaches the adsorbed film.

Figure 8b provides a closer look at the results of the microscale model. The two-way coupling between the microscale model and the CFD simulation allows the evaporation mass flux to influence the wall temperatures. Mass flux in the microscale model increases rapidly until the effects of disjoining pressure dominate the system, causing the evaporation rate to plummet to zero, forming an adsorbed film. The phase change induced Marangoni stress [92] and disjoining pressure impact the shape of the liquid-vapor interface. Figure 9 shows the interface shape in the transition thin film region. Interface shape predicted by the microscale model shows good agreement with the Young-Laplace equation (Equation (2)) away from the solid wall; however, the solutions deviate near the wall. Adsorbed film thicknesses of 100–128 nm and 62–75 nm are obtained for the SS 316 and Al 6061 cells, respectively.

In the present study, a *cutoff* distance of 10 μm was chosen to maintain consistency with prior studies [16,49,90,92]. However, this measure is arbitrary and can be adjusted to best fit the application of the model. The low contact angle of Hydrogen causes mesh cells in the liquid phase to become skewed as the meniscus approaches the cutoff region. This results in higher variance in the macroscale evaporation calculations. Mass flux data from the CFD mesh cells is shown as blue dots in Figure 8a and can be seen deviating from the mean value closer to the *cutoff*. This computational limit prohibits a smaller *cutoff* length from being used. Larger *cutoff* distances were tested and were found to

reduce the variance. Conversely, the choice of the *cutoff* length dictates the starting film height for the microscale model, where the lubrication approximation forms the basis of the hydrodynamic model. Therefore, a larger *cutoff* would increase the aspect ratio of the region, making the lubrication approximation invalid. A *cutoff* distance of 10 µm is found to be optimal.

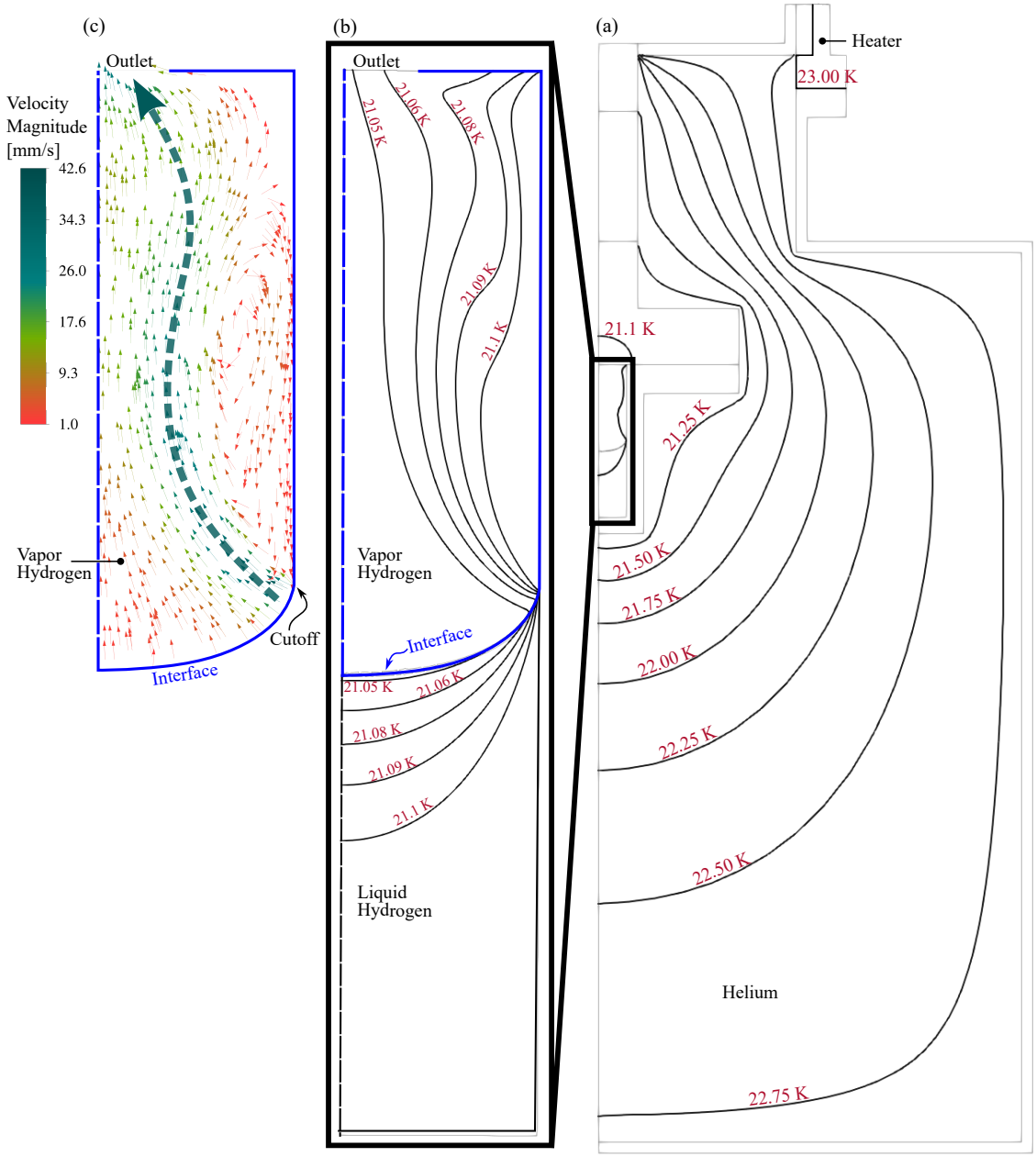

Figure 7. CFD results for the 10 mm Al test cell (tc4 run 1) are shown. (**a**) Contour lines showing the gradient in temperature from the heater to the test cell. (**b**) Inside the test cell, a temperature gradient results from the evaporative cooling caused by the non-uniform mass flux. (**c**) In the vapor phase, the evaporating mass leaves the interface and flows towards the pressure outlet at the top of the test cell. Higher evaporation velocities are seen near the solid wall due to the high evaporation flux from the transition thin film region. This results in a jet-like flow from the contact line to the central outlet at the top, as indicated by the dashed arrow.

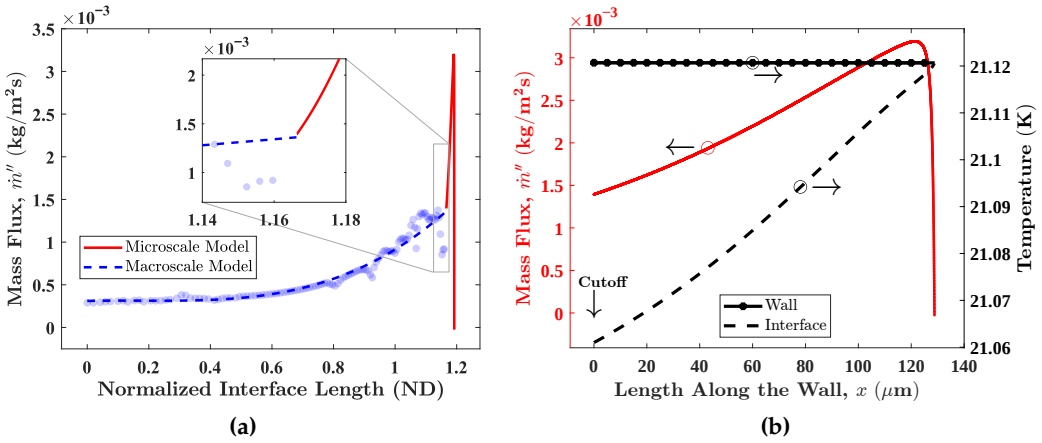

Figure 8. Results of the evaporation models. (**a**) Mass flux from the microscale and macroscale models is shown along the normalized interface length, defined as the ratio of the position along the interface to the test cell radius (Figure 4). The horizontal axis ranges from the center of the test cell to the solid wall and is normalized by the test cell's radius. Macroscale mass flux data from CFD cell centroids are shown in blue dots along with a polynomial fit. Mass flux increases closer to the solid wall and peaks in the transition thin film region before dropping to zero in the adsorbed film. (**b**) The microscale model resolves the peak in evaporation flux and variations in wall and interface temperatures.

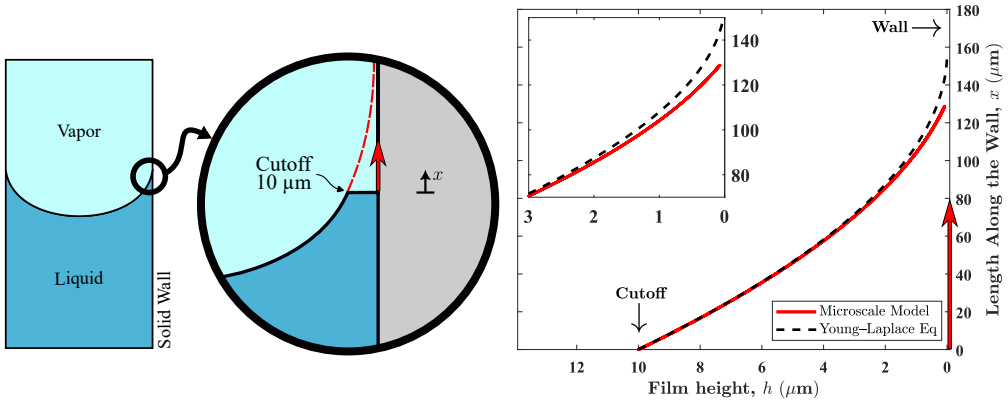

Figure 9. Interface shape obtained from the microscale model, in the 10 mm Al test cell (tc4 run 1), is compared with the solution from Equation (2). The solutions show agreement at the 10 μm *cutoff* distance, but deviate closer to the solid wall.

4.3. Comparison with Experiments

To compare the results of the multiscale model with experimental measurements, the mass flux distribution (Figure 8a) was integrated over the interfacial surface area to obtain the total evaporation rate.

$$\dot{m} = \iint \dot{m}''\, dA \approx \pi \sum_{j=1}^{N+N_\mu} \dot{m}''_j (r_{j+1}^2 - r_j^2) \tag{24}$$

where N is the number of CFD mesh cells along the meniscus and N_μ is the number of steps in the Runge-Kutta solution of the microscale model. Table 1 shows the total evaporation rate for three experimental runs in the 10 mm SS 316 test cell and four experimental runs in the 10 mm Al 6061 test cell. Evaporation rates from the multiscale model agree with experimental measurements within 1%. Contribution of the transition thin film region to the total evaporation rate is found to be between 24–27% in the SS 316 test cell and 14–18% in the Al 6061 test cell.

4.4. Comparison with Prior Models

Table 1 also compares the results of the present work with prior computational studies. The current study's results qualitatively concur with Bellur et al. [16]. However, a few key discrepancies can be observed in the contributions from the microscale and macroscale models. Bellur et al. [16]'s multiscale model was built with one-way coupling, i.e., the microscale evaporation did not influence the macroscale domain. This one-way coupling does not accurately account for the relative contributions from the microscale and macroscale models. This is clearly seen in the SS 316 test cell, where the current two-way coupled model predicts a higher contribution from the microscale region compared to the one-way coupled model by Bellur et al. [16]. This is attributed to the relatively low thermal conductivity and high heat capacity of SS 316 when compared to Al 6061. This results in reduced and hindered heat transfer, higher wall temperatures, and severe maldistribution despite enhanced evaporation (refer to the wall temperatures in Figure 10). In contrast, Al 6061 has much higher thermal conductivity and exhibits lesser variation in wall temperature, leading to a more moderate microscale evaporation contribution that matches with Bellur et al. [16]. This indicates that two-way coupling of the evaporation models is critical in cases where the solid wall exhibits lower thermal conductivity, but may suffice in ultra-low evaporation cases where the thermal conductivity is high.

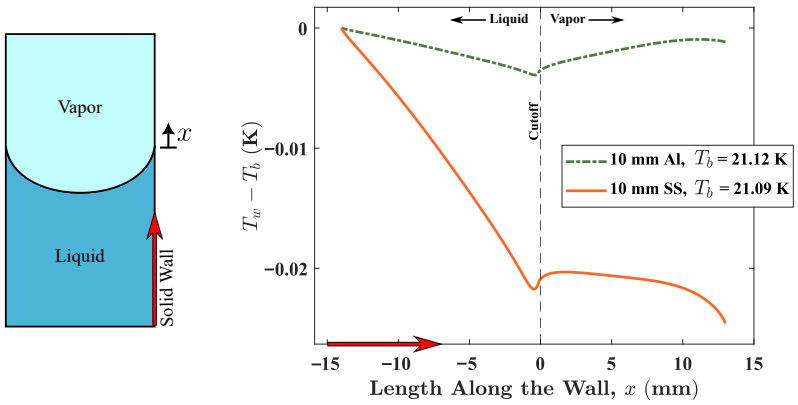

Figure 10. The variation in scaled wall temperatures with the bottom wall temperature (T_b) along the inside wall for both SS 316 (tc2) and Al 6061 (tc4) cells are shown. The location of *cutoff* is marked at $x = 0$. The positive x-direction denotes the vapor phase and the negative x-direction denotes the liquid phase. A localized drop in temperature is seen around the *cutoff* due to the high evaporative cooling caused by the transition thin film. The localized cooling in the SS 316 cell is more pronounced due to the lower thermal conductivity. This suggests a higher thin film contribution in the SS 316 cell compared to the Al 6061 cell.

Comparison with Yasin and Bellur [49] highlights the issue of overprediction with bulk-only evaporation models. In such models, the microscale contribution is completely ignored, and the contribution from the macroscale is artificially overpredicted to compensate for this shortcoming.

4.5. Novelty and Code Availability

In this work, we have developed a two-way coupled multiscale evaporation model housed inside a popular commercially available CFD software—Ansys Fluent^{TM}. The model incorporates a spatially varying mass flux using accommodation coefficients that are computed in situ from macroscale CFD parameters. This is a significant improvement over prior models that use this coefficient as a tuning parameter that is varied over several orders of magnitude [44,46,49–51]. Here, we find that the α has a value between 0.584–0.586 and varies minimally over the interface. Enhanced thin film evaporation at the contact

line is captured through a subgrid microscale model (using Runge–Kutta solvers) and is coupled with the bulk CFD using custom User-Defined Functions (UDFs). The model accurately captures the non-monotonic variation in mass flux across the multiscale interface. Continuity in the mass flux between the macroscale and microscale models is achieved. The multiscale model is built such that it only requires global parameters such as vapor pressure, Bond number, container geometry, and appropriate thermal fluid properties, all of which are typically known a priori. The primary novelty in the current work is that there is no need for arbitrary tuning parameters to match experimental results or attain numerical convergence, as has been the case with prior models. To the authors' best knowledge, this is the first two-way coupled multiscale evaporation model (with thin film contribution) housed inside a commercial CFD software and is devoid of explicit tuning parameters. Furthermore, the present model can be easily added to an existing CFD framework through custom UDFs. We provide our UDFs for implementation in Ansys Fluent^{TM}, but this can be replicated for other CFD environments. Details regarding the UDF code, the compilation process, and implementation can be found in the associated GitHub repository (v1.0) [93].

5. Summary and Conclusions

As the world transitions to green fuels, such as Hydrogen, evaporative modeling is vital, particularly for long-term storage and transportation in its cryogenic liquid state. During the Space Shuttle Program, over 40% of the liquid Hydrogen was lost to vaporization during storage and transportation [12]. A robust multiscale evaporation model is needed to solve this problem [14]. However, existing evaporation models are riddled with assumptions and simplifications that limit their applicability and overall confidence. Drawbacks include, but are not limited to: arbitrarily chosen accommodation coefficients, guessed boundary conditions, neglect of contact line phenomena, etc. These cause issues such as extensive tuning and overprediction of bulk evaporation, leading to ill-informed designs for fuel storage technology. The present study attempts to address these issues by developing multiscale, two-way coupled evaporation model devoid of arbitrary tuning such that it can be easily integrated into the Ansys Fluent^{TM} framework. The present study employs the following key features to provide an accurate modeling of Hydrogen fuel evaporation:

- Two-way coupling between the microscale thin film model and the macroscale CFD model.
- Numerical conditioning that also improves the time complexity of the simulation.
- Transition state theory-based non-uniform mass accommodation coefficients.
- Physics-based parameter, γ for approximating temperature in the Knudsen layer.

The study has shown the importance of contact line phenomena as evidenced by the high contribution (up to 27%) from the microscale thin film region near the wall. Further, the wall temperatures in the vicinity of the contact line are non-uniform, contrary to many prior models. A numerical treatment of the multi-scale approach is discussed, highlighting the complexity of coupling the different length scales and methods to achieve stability across them. The results of the present study can be summarized as:

(a) The thin film region exhibits an enhanced evaporation mass flux. Peak mass flux in the thin film is found to be close to an order of magnitude greater than the macroscale bulk region.

(b) The thin film contribution was observed to be between 14–27% of the total evaporation rate.

(c) One-way coupling (where the bulk influences the microscale thin film but not vice-versa) under-predicts the contribution from the microscale thin film region for cases

where the solid wall has low thermal conductivity, such as stainless steel. For such materials, the two-way coupled model is recommended.

(d) The accommodation coefficients are strictly allowed to vary along the liquid-vapor interface, but the variation is found to be minimal (<1%) for the cases tested in the present study.

(e) The UDF code package is made available to facilitate replication and serve as a starting point for further studies.

Author Contributions: Conceptualization, A.Y. and K.B.; Formal Analysis, S.P. and A.Y.; Funding Acquisition, K.B.; Methodology, S.P. and A.Y.; Supervision, K.B.; Writing—Original Draft, S.P. and A.Y.; Writing—Review & Editing, K.B. All authors have read and agreed to the published version of the manuscript.

Funding: This work was partly supported by the NSF CAREER Award (#CBET2339757). The authors acknowledge support from the University of Cincinnati through a Graduate Incentive Award for Ayaaz Yasin and an ASTRO (Armstrong Institute for Space, Technology, and Research) fellowship for Saaras Pakanati.

Data Availability Statement: The raw data supporting the conclusions of this article will be made available by the authors on request. The experimental data were obtained from a publicly available repository Bellur et al. [36]. The code developed in the present study is openly available in the associated GitHub repository at: https://github.com/UC-Lab-For-Interfacial-Dynamics/EMEM/ (accessed on 7 December 2025).

Conflicts of Interest: The authors declare no conflicts of interest.

Nomenclature

A	Area	m^2
$\mathcal{A}$	Hamaker constant	J
Bo	Bond number	–
c	Parameters in Equation (4)	–
c_p	Specific heat	J/kg K
$\tilde{f}$	Dimensionless height	–
h	Meniscus height	m
h_x	First Derivative of Meniscus height	–
h_{xx}	Second Derivative of Meniscus height	1/m
h_{fg}	Enthalpy of vaporization	J/kg
H_s	Sensible Enthalpy	J/kg
J_{M}	Area-averaged molar flux	mol/m^2 s
k	Thermal conductivity	W/m K
$\dot{m}$	Phase change rate	kg/s
$\dot{m}''$	Phase change mass flux	kg/m^2 s
M	Molar mass	kg/mol
N	Number of Runge-Kutta steps	–
p	Pressure	Pa
r	Radius	m
$\tilde{r}$	Dimensionless radial distance	–
R	Radius of test cell	m
$\overline{R}$	Universal gas constant	J/mol K
S_{m}	Mass source term	kg/m^3 s
S_{HB}	Heat balance source term	W/m^3
T	Temperature	K
$\overline{T_i}$	Mass flux–averaged interface temperature	K
V	Volume	m^3
x	Distance along thin film	m

Greek Symbols

α	Accommodation coefficient	–
β	Ratio of evaporation and condensation coefficients	–
γ	Vapor temperature reduction factor	–
δ	Mesh size	μm
θ	Contact angle	rad
κ	Surface curvature	1/m
μ	Viscosity	Pa-s
λ	Parameter in Equation (2)	–
Π	Disjoining pressure	Pa
ρ	Density	kg/m^3
σ	Surface tension	N/m
Γ	Mass Flow	kg/s
ψ	Parameter in Equation (2)	–
$\vec{u}$	Velocity	m/s

Subscripts and Superscripts

cell	Mesh cell
c	Condensation
HB	Heat balance
i	Interface
l	Liquid
LH	Latent heat
m	Mass
M	Molar
ref	Reference
sat	Saturation
surf	Interfacial surface
tf	Thin film
v	Vapor

References

1. Clark, J.D. *Ignition! An Informal History of Liquid Rocket Propellants*; Rutgers University Press: New Brunswick, NJ, USA, 1972.
2. Cecere, D.; Giacomazzi, E.; Ingenito, A. A Review on Hydrogen Industrial Aerospace Applications. *Int. J. Hydrogen Energy* **2014**, *39*, 10731–10747. [CrossRef]
3. Staffell, I.; Scamman, D.; Abad, A.V.; Balcombe, P.; Dodds, P.E.; Ekins, P.; Shah, N.; Ward, K.R. The Role of Hydrogen and Fuel Cells in the Global Energy System. *Energy Environ. Sci.* **2019**, *12*, 463–491. [CrossRef]
4. Oliveira, A.M.; Beswick, R.R.; Yan, Y. A Green Hydrogen Economy for a Renewable Energy Society. *Curr. Opin. Chem. Eng.* **2021**, *33*, 100701. [CrossRef]
5. Edwards, P.P.; Kuznetsov, V.L.; David, W.I.F.; Brandon, N.P. Hydrogen and Fuel Cells: Towards a Sustainable Energy Future. *Energy Policy* **2008**, *36*, 4356–4362. [CrossRef]
6. Struzhkin, V.V.; Militzer, B.; Mao, W.L.; Mao, H.k.; Hemley, R.J. Hydrogen Storage in Molecular Clathrates. *Chem. Rev.* **2007**, *107*, 4133–4151. [CrossRef]
7. Lubitz, W.; Tumas, W. Hydrogen: An Overview. *Chem. Rev.* **2007**, *107*, 3900–3903. [CrossRef]
8. Friedlander, A.; Zubrin, R.; Hardy, T.L. *Benefits of Slush Hydrogen for Space Missions*; Technical Report NASA-TM-104503; NASA: Washington, DC, SA, 1991.
9. Hardy, T.; Whalen, M. Technology Issues Associated with Using Densified Hydrogen for Spacevehicles. In Proceedings of the 28th Joint Propulsion Conference and Exhibit, Nashville, TN, USA, 6–8 July 1992. [CrossRef]
10. Mueller, P.; Durrant, T. Cryogenic Propellant Liquefaction and Storage for a Precursor to a Human Mars Mission. *Cryogenics* **1999**, *39*, 1021–1028. [CrossRef]
11. Hartwig, J.W. *Liquid Acquisition Devices for Advanced In-Space Cryogenic Propulsion Systems*; Academic Press: Cambridge, MA, USA, 2014.
12. Partridge, J.K. Fractional Consumption of Liquid Hydrogen and Liquid Oxygen during the Space Shuttle Program. In Proceedings of the Advances in Cryogenic Engineering: Transactions of the Cryogenic Engineering Conference—CEC, Spokane, WA, USA, 13–17 June 2012; Volume 57, pp. 1765–1770. [CrossRef]

13. Kassemi, M.; Kartuzova, O.; Hylton, S. Validation of Two-Phase CFD Models for Propellant Tank Self-Pressurization: Crossing Fluid Types, Scales, and Gravity Levels. *Cryogenics* **2018**, *89*, 1–15. [CrossRef]
14. Simonini, A.; Dreyer, M.; Urbano, A.; Sanfedino, F.; Himeno, T.; Behruzi, P.; Avila, M.; Pinho, J.; Peveroni, L.; Gouriet, J.B. Cryogenic Propellant Management in Space: Open Challenges and Perspectives. *npj Microgravity* **2024**, *10*, 34. [CrossRef]
15. Srikanth, P.; Collicott, S.H. Effect of Temperature and Pressure Measurement Uncertainties on Phase Change Calculations with Liquid Hydrogen. In *AIAA Propulsion and Energy 2019 Forum*; American Institute of Aeronautics and Astronautics: Reston, VA, USA, 2019. [CrossRef]
16. Bellur, K.; Médici, E.F.; Choi, C.K.; Hermanson, J.C.; Allen, J.S. Multiscale Approach to Model Steady Meniscus Evaporation in a Wetting Fluid. *Phys. Rev. Fluids* **2020**, *5*, 024001. [CrossRef]
17. Struchtrup, H. Mass and Heat Transfer Resistivities at Liquid–Vapor Interfaces: Beyond the Ideal Gas. *Int. J. Heat Mass Transf.* **2026**, *256*, 127943. [CrossRef]
18. Ranjan, R.; Murthy, J.Y.; Garimella, S.V. A Microscale Model for Thin-Film Evaporation in Capillary Wick Structures. *Int. J. Heat Mass Transf.* **2011**, *54*, 169–179. [CrossRef]
19. Dhavaleswarapu, H.K.; Murthy, J.Y.; Garimella, S.V. Numerical Investigation of an Evaporating Meniscus in a Channel. *Int. J. Heat Mass Transf.* **2012**, *55*, 915–924. [CrossRef]
20. Wang, H.; Garimella, S.V.; Murthy, J.Y. An Analytical Solution for the Total Heat Transfer in the Thin-Film Region of an Evaporating Meniscus. *Int. J. Heat Mass Transf.* **2008**, *51*, 6317–6322. [CrossRef]
21. Zuo, Z.; Zhu, W.; Huang, Y.; Wang, L.; Tong, L. A Review of Cryogenic Quasi-Steady Liquid-Vapor Phase Change: Theories, Models, and State-of-the-Art Applications. *Int. J. Heat Mass Transf.* **2023**, *205*, 123916. [CrossRef]
22. Hertz, H. Ueber die Verdunstung der Flüssigkeiten, insbesondere des Quecksilbers, im luftleeren Raume. *Ann. Der Phys.* **1882**, *253*, 177–193. [CrossRef]
23. Knudsen, M. Die maximale Verdampfungsgeschwindigkeit des Quecksilbers. *Ann. Der Phys.* **1915**, *352*, 697–708. [CrossRef]
24. Schrage, R. A Theoretical Study of Interphase Mass Transfer. PhD Thesis, Columbia University Press, New York, NY, USA, 1953.
25. Wayner, P.; Kao, Y.; LaCroix, L. The Interline Heat-Transfer Coefficient of an Evaporating Wetting Film. *Int. J. Heat Mass Transf.* **1976**, *19*, 487–492. [CrossRef]
26. Bellur, K.; Médici, E.F.; Hermanson, J.C.; Choi, C.K.; Allen, J.S. Modeling Liquid–Vapor Phase Change Experiments: Cryogenic Hydrogen and Methane. *Colloids Surfaces Physicochem. Eng. Asp.* **2023**, *675*, 131932. [CrossRef]
27. Chakrabarti, U.; Allen, J.S.; Bellur, K. Investigating the Inequality of Phase Change Coefficients Using ISS Experimental Data. *Nanoscale Microscale Thermophys. Eng.* **2025**, *29*, 139–158. [CrossRef]
28. Marek, R.; Straub, J. Analysis of the Evaporation Coefficient and the Condensation Coefficient of Water. *Int. J. Heat Mass Transf.* **2001**, *44*, 39–53. [CrossRef]
29. Persad, A.H.; Ward, C.A. Expressions for the Evaporation and Condensation Coefficients in the Hertz-Knudsen Relation. *Chem. Rev.* **2016**, *116*, 7727–7767. [CrossRef]
30. Eames, I.; Marr, N.; Sabir, H. The Evaporation Coefficient of Water: A Review. *Int. J. Heat Mass Transf.* **1997**, *40*, 2963–2973. [CrossRef]
31. Paul, B. Compilation of Evaporation Coefficients. *ARS J.* **1962**, *32*, 1321–1328. [CrossRef]
32. Cheng, S.; Lechman, J.B.; Plimpton, S.J.; Grest, G.S. Evaporation of Lennard-Jones Fluids. *J. Chem. Phys.* **2011**, *134*, 224704. [CrossRef]
33. Ishiyama, T.; Yano, T.; Fujikawa, S. Molecular Dynamics Study of Kinetic Boundary Condition at an Interface between Argon Vapor and Its Condensed Phase. *Phys. Fluids* **2004**, *16*, 2899–2906. [CrossRef]
34. Liang, Z.; Biben, T.; Keblinski, P. Molecular Simulation of Steady-State Evaporation and Condensation: Validity of the Schrage Relationships. *Int. J. Heat Mass Transf.* **2017**, *114*, 105–114. [CrossRef]
35. Bellur, K.; Médici, E.F.; Hussey, D.S.; Jacobson, D.L.; LaManna, J.; Leão, J.B.; Scherschligt, J.; Hermanson, J.C.; Choi, C.K.; Allen, J.S. Results from Neutron Imaging Phase Change Experiments with LH2 and LCH4. *Cryogenics* **2022**, *125*, 103517. [CrossRef]
36. Bellur, K.; Medici, E.F.; Hussey, D.S.; Jacobson, D.L.; LaManna, J.; Leao, J.B.; Scherschligt, J.; Hermanson, J.C.; Choi, C.K.; Allen, J.S. Data from Cryo-Neutron Phase Change Experiments with LH2 and LCH4. *Data Brief* **2022**, *43*, 108474. [CrossRef]
37. Bellur, K.; Konduru, V.; Medici, E.F.; Hussey, D.S.; Jacobson, D.L.; LaManna, J.M.; Allen, J.S.; Choi, C.K. Visualization of the Evaporation and Condensation Phenomena in Cryogenic Propellants. *J. Flow Vis. Image Process.* **2016**, *23*, 137–156. [CrossRef]
38. Bellur, K.; Konduru, V.; Kulshrestha, M.; Tyrewala, D.; Medici, E.; Allen, J.S.; Choi, C.K.; Hussey, D.S.; Jacobson, D.C.; Leão, J.B.; et al. Contact Angle Measurement of Liquid Hydrogen (LH2) in Stainless Steel and Aluminum Cells. *J. Heat Transf.* **2016**, *138*, 020904. [CrossRef]
39. Concus, P. Static Menisci in a Vertical Right Circular Cylinder. *J. Fluid Mech.* **1968**, *34*, 481–495. [CrossRef]
40. Plawsky, J.L.; Ojha, M.; Chatterjee, A.; Wayner, P.C. Review of the Effects of Surface Topography, Surface Chemistry, and Fluid Physics on Evaporation at the Contact Line. *Chem. Eng. Commun.* **2008**, *196*, 658–696. [CrossRef]
41. de Gennes, P.G. Wetting: Statics and Dynamics. *Rev. Mod. Phys.* **1985**, *57*, 827–863. [CrossRef]

42. Ajaev, V.S. Spreading of Thin Volatile Liquid Droplets on Uniformly Heated Surfaces. *J. Fluid Mech.* **2005**, *528*, 279–296. [CrossRef]
43. Plawsky, J.L.; Fedorov, A.G.; Garimella, S.V.; Ma, H.B.; Maroo, S.C.; Chen, L.; Nam, Y. Nano- and Microstructures for Thin-Film Evaporation—A Review. *Nanoscale Microscale Thermophys. Eng.* **2014**, *18*, 251–269. [CrossRef]
44. Tan, Z.; Cao, Z.; Chu, W.; Wang, Q. Improvement on Evaporation-Condensation Prediction of Lee Model via a Temperature Deviation Based Dynamic Correction on Evaporation Coefficient. *Case Stud. Therm. Eng.* **2023**, *48*, 103147. [CrossRef]
45. Yasin, A. Computational Modeling of Evaporation Without Tuning Coefficients. Master's Thesis, University of Cincinnati, Cincinnati, OH, USA, 2024.
46. Lee, W.H. *Pressure Iteration Scheme for Two-Phase Flow Modeling*; Technical Report LA-UR 79-975; World Scientific Connect: Singapore, 1979; pp. 407–431.
47. Ansys Fluent 12.0/12.1 Documentation. Available online: https://www.afs.enea.it/project/neptunius/docs/fluent/index.htm (accessed on 7 December 2025).
48. OpenFoam v2112 Documentation. Available online: https://www.openfoam.com/documentation/guides/v2206/doc/index.html (accessed on 7 December 2025).
49. Yasin, A.; Bellur, K. Computational Modeling of Evaporation without Tuning Coefficients. *Appl. Therm. Eng.* **2025**, *276*, 126807. [CrossRef]
50. Kharangate, C.R.; Mudawar, I. Review of Computational Studies on Boiling and Condensation. *Int. J. Heat Mass Transf.* **2017**, *108*, 1164–1196. [CrossRef]
51. Kim, D.G.; Jeon, C.H.; Park, I.S. Comparison of Numerical Phase-Change Models through Stefan Vaporizing Problem. *Int. Commun. Heat Mass Transf.* **2017**, *87*, 228–236. [CrossRef]
52. Wang, X.; Yao, H.; Li, J.; Wang, Y.; Zhu, Y. Experimental and Numerical Investigation on Heat Transfer Characteristics of Ammonia Thermosyhpons at Shallow Geothermal Temperature. *Int. J. Heat Mass Transf.* **2019**, *136*, 1147–1159. [CrossRef]
53. Liang, Z.; Keblinski, P. Molecular Simulation of Steady-State Evaporation and Condensation in the Presence of a Non-Condensable Gas. *J. Chem. Phys.* **2018**, *148*, 064708. [CrossRef]
54. Liang, Z.; Chandra, A.; Bird, E.; Keblinski, P. A Molecular Dynamics Study of Transient Evaporation and Condensation. *Int. J. Heat Mass Transf.* **2020**, *149*, 119152. [CrossRef]
55. Akkus, Y.; Gurer, A.T.; Bellur, K. Drifting Mass Accommodation Coefficients: In Situ Measurements from a Steady State Molecular Dynamics Setup. *Nanoscale Microscale Thermophys. Eng.* **2020**, *25*, 25–45. [CrossRef]
56. Gatapova, E.Y. Evaporation into Half-Space: Experiments with Water at the Molecular Mean Free Path Scale. *Phys. Fluids* **2024**, *36*, 091707. [CrossRef]
57. Ajaev, V.S. *Interfacial Fluid Mechanics: A Mathematical Modeling Approach*; Springer: Boston, MA, USA, 2012. [CrossRef]
58. Knüpfer, H. Classical Solutions for a Thin-Film Equation. Ph.D. Thesis, Rheinische Friedrich-Wilhelms-Universität, Bonn, Germany, 2008.
59. Craster, R.V.; Matar, O.K. Dynamics and Stability of Thin Liquid Films. *Rev. Mod. Phys.* **2009**, *81*, 1131–1198. [CrossRef]
60. Giacomelli, L.; Otto, F. Rigorous Lubrication Approximation. *Interfaces Free Boundaries Math. Anal. Comput. Appl.* **2003**, *5*, 483–529. [CrossRef]
61. Potash, M.; Wayner, P. Evaporation from a Two-Dimensional Extended Meniscus. *Int. J. Heat Mass Transf.* **1972**, *15*, 1851–1863. [CrossRef]
62. Hocking, L.M. On Contact Angles in Evaporating Liquids. *Phys. Fluids* **1995**, *7*, 2950–2955. [CrossRef]
63. Morris, S.J.S. A Phenomenological Model for the Contact Region of an Evaporating Meniscus on a Superheated Slab. *J. Fluid Mech.* **2000**, *411*, 59–89. [CrossRef]
64. Moosman, S.; Homsy, G.M. Evaporating Menisci of Wetting Fluids. *J. Colloid Interface Sci.* **1980**, *73*, 212–223. [CrossRef]
65. Ajaev, V.S.; Homsy, G.; Morris, S. Dynamic Response of Geometrically Constrained Vapor Bubbles. *J. Colloid Interface Sci.* **2002**, *254*, 346–354. [CrossRef]
66. Soria, F.; Woodruff, E.; Fordon, A.G.; Xu, Y.; Putnam, S.A. Multiscale Modeling of Microdroplet Evaporation and Single Pulse Spray Cooling. *Fluid Dyn. Res.* **2025**, *57*, 025504. [CrossRef]
67. Lakew, E.; Sarchami, A.; Giustini, G.; Kim, H.; Bellur, K. Thin Film Evaporation Modeling of the Liquid Microlayer Region in a Dewetting Water Bubble. *Fluids* **2023**, *8*, 126. [CrossRef]
68. Stephan, P.C.; Busse, C.A. Analysis of the Heat Transfer Coefficient of Grooved Heat Pipe Evaporator Walls. *Int. J. Heat Mass Transf.* **1992**, *35*, 383–391. [CrossRef]
69. DasGupta, S.; Schonberg, J.A.; Kim, I.Y.; Wayner, P.C. Use of the Augmented Young-Laplace Equation to Model Equilibrium and Evaporating Extended Menisci. *J. Colloid Interface Sci.* **1993**, *157*, 332–342. [CrossRef]
70. Schonberg, J.A.; DasGupta, S.; Wayner, P.C. An Augmented Young-Laplace Model of an Evaporating Meniscus in a Microchannel with High Heat Flux. *Exp. Therm. Fluid Sci.* **1995**, *10*, 163–170. [CrossRef]
71. Park, K.; Noh, K.J.; Lee, K.S. Transport Phenomena in the Thin-Film Region of a Micro-Channel. *Int. J. Heat Mass Transf.* **2003**, *46*, 2381–2388. [CrossRef]

72. Wang, H.; Garimella, S.V.; Murthy, J.Y. Characteristics of an Evaporating Thin Film in a Microchannel. *Int. J. Heat Mass Transf.* **2007**, *50*, 3933–3942. [CrossRef]
73. Abolmaali, A.M.; Bayat, M.; Hattel, J. A Multiscale Analytical-Numerical Method for the Coupled Heat and Mass Transfer in the Extended Meniscus Region Considering Thin-Film Evaporation in Microchannels. *Int. J. Heat Mass Transf.* **2024**, *222*, 125145. [CrossRef]
74. Du, S.Y.; Zhao, Y.H. Numerical Study of Conjugated Heat Transfer in Evaporating Thin-Films near the Contact Line. *Int. J. Heat Mass Transf.* **2012**, *55*, 61–68. [CrossRef]
75. Kou, Z.H.; Lv, H.T.; Zeng, W.; Bai, M.L.; Lv, J.Z. Comparison of Different Analytical Models for Heat and Mass Transfer Characteristics of an Evaporating Meniscus in a Micro-Channel. *Int. Commun. Heat Mass Transf.* **2015**, *63*, 49–53. [CrossRef]
76. Akkuş, Y.; Dursunkaya, Z. A New Approach to Thin Film Evaporation Modeling. *Int. J. Heat Mass Transf.* **2016**, *101*, 742–748. [CrossRef]
77. Barrett, J.A.; Ajaev, V.S. Modeling of Moving Liquid-Vapor Interfaces in the Constrained Vapor Bubble System. *Microgravity Sci. Technol.* **2019**, *31*, 685–692. [CrossRef]
78. Mostafazade Abolmaali, A.; Bayat, M.; Hattel, J. Thin-Film Evaporation in Microchannels: A Combined Analytical and Computational Fluid Dynamics Approach to Assessing Meniscus Curvature Impact. *Int. J. Therm. Sci.* **2025**, *208*, 109455. [CrossRef]
79. Wee, S.K.; Kihm, K.D.; Hallinan, K.P. Effects of the Liquid Polarity and the Wall Slip on the Heat and Mass Transport Characteristics of the Micro-Scale Evaporating Transition Film. *Int. J. Heat Mass Transf.* **2005**, *48*, 265–278. [CrossRef]
80. Do, K.H.; Kim, S.J.; Garimella, S.V. A Mathematical Model for Analyzing the Thermal Characteristics of a Flat Micro Heat Pipe with a Grooved Wick. *Int. J. Heat Mass Transf.* **2008**, *51*, 4637–4650. [CrossRef]
81. Chen, X.; Qi, C.; Wang, W.; Miao, J.; Zhang, H. Investigation of Interface Profiles in Meshed Wicks and Related Evaporation Characteristics. *Int. J. Therm. Sci.* **2022**, *177*, 107522. [CrossRef]
82. Gökçe, G.; Kurt, C.; Odabaşı, G.; Dursunkaya, Z.; Çetin, B. Comprehensive Three-Dimensional Hydrodynamic and Thermal Modeling of Steady-State Operation of a Flat Grooved Heat Pipe. *Int. J. Multiph. Flow* **2023**, *160*, 104370. [CrossRef]
83. Nagayama, G.; Tsuruta, T. A General Expression for the Condensation Coefficient Based on Transition State Theory and Molecular Dynamics Simulation. *J. Chem. Phys.* **2003**, *118*, 1392–1399. [CrossRef]
84. Barclay, P.L.; Lukes, J.R. Curvature Dependence of the Mass Accommodation Coefficient. *Langmuir* **2019**, *35*, 6196–6202. [CrossRef]
85. Nagayama, G.; Takematsu, M.; Mizuguchi, H.; Tsuruta, T. Molecular Dynamics Study on Condensation/Evaporation Coefficients of Chain Molecules at Liquid–Vapor Interface. *J. Chem. Phys.* **2015**, *143*, 014706. [CrossRef]
86. Derjaguin, B.; Zorin, Z. Optical Study of the Adsorption and Surface Condensation of Vapours in the Vicinity of Saturation on a Smooth Surface. *Prog. Surf. Sci.* **1992**, *40*, 83–117. [CrossRef]
87. Israelachvili, J.N. *Intermolecular and Surface Forces*, 3rd ed.; Elsevier: Amsterdam, The Netherlands; Academic Press: Burlington, MA, USA, 2011.
88. Dai, B.; Leal, L.G.; Redondo, A. Disjoining Pressure for Nonuniform Thin Films. *Phys. Rev. E* **2008**, *78*, 061602. [CrossRef] [PubMed]
89. NIST Chemistry WebBook. NIST Standard Reference Database 69. 1997. Available online: https://webbook.nist.gov/chemistry/ (accessed on 7 December 2025).
90. Bellur, K.; Médici, E.; Hermanson, J.; Choi, C.; Allen, J. Determining Solid-Fluid Interface Temperature Distribution during Phase Change of Cryogenic Propellants Using Transient Thermal Modeling. *Cryogenics* **2018**, *91*, 103–111. [CrossRef]
91. Khrustalev, D.; Faghri, A. Fluid Flow Effects in Evaporation From Liquid–Vapor Meniscus. *J. Heat Transf.* **1996**, *118*, 725–730. [CrossRef]
92. Chakrabarti, U.; Yasin, A.; Bellur, K.; Allen, J.S. An Investigation of Phase Change Induced Marangoni-dominated Flow Patterns Using the Constrained Vapor Bubble Data from ISS Experiments. *Front. Space Technol.* **2023**, *4*, 1263496. [CrossRef]
93. UC Lab for Interfacial Dynamics. Embedded Multiscale Evaporation Model. Available online: https://github.com/UC-Lab-For-Interfacial-Dynamics/EMEM/ (accessed on 7 December 2025).